Transp Porous Med (2012) 91:479–508
DOI 10.1007/s11242-011-9856-0

Deep Bed Filtration Modelling of Formation Damage Due to Particulate Invasion from Drilling Fluids

Edo S. Boek · Christopher Hall · Philippe M. J. Tardy

Received: 15 March 2011 / Accepted: 25 August 2011 / Published online: 28 September 2011

Abstract A Deep Bed Filtration model has been developed to quantify the effect of solids invasion from drilling fluids on the permeability of rock formations. The calculated particle-trapping profiles are compared directly with experimental profiles from scanning electron microscopy and synchrotron *X*-ray diffraction tomography mapping. The computed permeability reduction as a consequence of particle invasion is in broad agreement with experiment. Backflow was modelled by reversing the flow rate, starting off with a situation where all particles either remain trapped or are all released. It appears that the experimentally observed 30% release of particles upon backflow is reproducible within the limits of the two extreme cases. When erosion is included in the model, a peak in the backflow pressure time series can be observed. This peak may be correlated with the experimentally observed flow initiation pressure, which is the backflow pressure needed to initiate flow after initial inflow filtration. Finally, we conclude that internal reservoir damage, within the limits of our 1-D single phase DBF model, may contribute to the experimentally observed flow initiation pressure.

Keywords Deep bed filtration · Formation damage · Drilling fluids

E. S. Boek (✉)
Department of Chemical Engineering, Imperial College, London SW7 2AZ, UK
e-mail: e.boek@imperial.ac.uk

E. S. Boek
Schlumberger Cambridge Research, High Cross, Madingley Road, Cambridge CB3 0EL, UK

C. Hall
School of Engineering, University of Edinburgh, Edinburgh EH9 3JL, UK

P. M. J. Tardy
Schlumberger Oilfield Eastern Ltd, PO Box 9056, Plot 67, Street 349, 61001 Al Ahmadi, Kuwait

1 Introduction

The transport, capture and erosion of particulates in porous media are of significant importance in the oil production process. A few areas of particular concern are the following:

- sand production from wells in weak rock formations due to high production rates
- formation damage due to migration and deposition of fines during oil production
- impairment of downhole logging measurements due to particulate invasion from drilling fluids
- formation damage due to particulate invasion from drilling fluids

In this paper, we will focus on the issue last-mentioned. During drilling operations, cross-flow (or dynamic) filtration of drilling fluid will occur into the surrounding permeable rock formation. Fluid loss from the drilling mud is minimised by the creation of a low permeability filter cake at the surface of the wellbore. Formation damage occurs when particulates from the drilling mud (such as drill solids, weighting agents but also soft particles like polymers) invade into the reservoir rock, thus plugging pores and forming an internal filter cake. Backflow with hydrocarbons may partially clean up the filter cake, but in general, the permeability of reservoir formations will be seriously impaired such that hydrocarbon production is reduced. For this reason, a large amount of experimental work has been done to control particle deposition in porous media. The size of the solids relative to the grains in the reservoir rock determines whether the solids will invade or bridge on the rock surface. Figures 1 and 2 show invasion and bridging of a fine ($d_{50} = 4\,\mu\text{m}$) and a coarse ($d_{50} = 40\,\mu\text{m}$) calcium carbonate, respectively, on a Ketton limestone (pore $d_{50} = 60\,\mu\text{m}$) (Bailey et al. 1999).

It is the goal of this paper to model to what extent solid particulates penetrate into the reservoir rock during the filtration process and how this influences the rock permeability. We will compare our trapped particle profiles with data from synchrotron X-ray and electron microscopy experiments. Also, we will investigate to what extent backflow can be expected to clean up part of the formation damage and whether internal reservoir damage contributes to the flow initiation pressure (FIP). The FIP is defined as the backflow pressure required to initiate flow, which is believed to be associated with filtercake failure (Bailey et al. 1998).

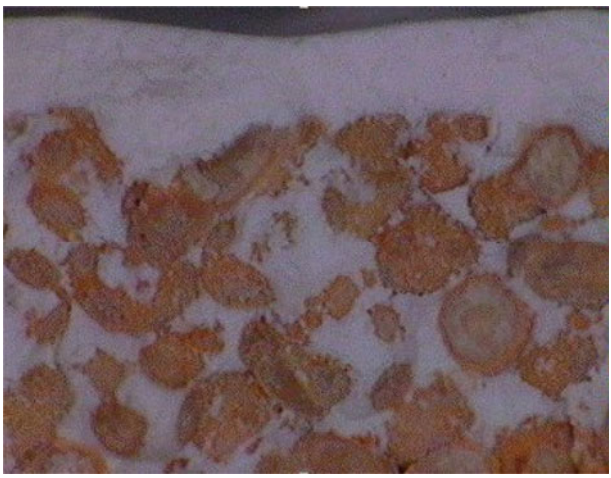

Fig. 1 Invasion of ultra-fine carbonate C1 ($d_{50} = 4\,\mu\text{m}$) on a Ketton limestone core (with pore $d_{50} = 60\,\mu\text{m}$)

Fig. 2 Bridging with a coarse carbonate solid ($d_{50} = 40\,\mu\text{m}$) on a Ketton limestone core (with pore $d_{50} = 60\,\mu\text{m}$)

Models of particulate processes in porous media can be subdivided into macroscopic and microscopic models. On a microscopic scale, the porous medium is represented by a collection of interconnected pores. This is the case in network models, which have been used to study filtration processes of solid particles (Sharma and Yortsos 1987a,b,c; Rege and Fogler 1988) as well as emulsion drops (Rege and Fogler 1987). Macroscopic/continuum models can be used as soon as the invading particles are much smaller than the pore throats, and all the relevant mechanisms describing the motion of the particles are upscaled from the microscopic to the continuum level. This is the approach we will follow here. In this paper, we will describe the development of a deep bed filtration (DBF) model to quantify the effect of solids invasion on permeability. We have assumed that the final form of the macroscopic equations for the DBF model is valid, without performing strict upscaling from the microscopic level. Then, validation of these equations is required by comparing the model predictions with experimental data. A review of early work on DBF filtration modelling is given in Herzig et al. (1970). These models describe particles moving in terms of concentration fields, without explicitly representing the pore space, and include the flow continuity equation, a mass balance equation and a kinetic equation for the porosity. Recently, the sand production problem in oil production as a consequence of erosion of sand particles has been successfully studied following a similar approach (Vardoulakis et al. 1996). Wennberg et al. (1996) studied band formation due to fines deposition in porous media.

Our results show that the calculated particle-trapping profile can be compared quantitatively with experimental profiles from scanning electron microscopy and synchrotron X-ray sources. The computed permeability reduction as a consequence of particle invasion is in broad agreement with experiment. Backflow was modelled by reversing the flow rate, starting off with situations where either all particles remain trapped or are all released. It appears that the experimentally observed 30% release of particles upon backflow is reproducible within the limits of the two extreme cases. When erosion is included in the model, a peak in the pressure profile can be observed. This peak may be correlated with the experimentally observed flow initiation pressure (FIP), which is the backflow pressure needed to initiate flow after initial inflow filtration. Finally, we conclude that internal reservoir damage, within the

limits of our 1-D single phase DBF model, may contribute to the experimentally observed flow initiation pressure.

2 Deep Bed Filtration Model

We consider a simple continuum model for particle trapping within the rock as a consequence of drilling fluid invasion. Particle trapping is a deep bed filtration process. We follow a phenomenological approach by postulating simple conservation laws and rate equations. Initially, we will consider a 1-D single-phase flow model, but the equations can be extended to more dimensions and more fluid phases. Note that we will consider only invasion of solid particulates in the current report, but the general approach described equally applies to invasion of soft condensed matter, such as polymers or emulsion droplets.

We denote c_p^e the volume fraction of element e in phase p. The elements under consideration are water ($e = w$), rock ($e = r$) and the particles ($e = p$). The phases are water ($p = w$) and rock ($p = r$). Before filtration, the rock porosity is equal to ϕ_0 and varies with time as particles become trapped. At later stages, the porosity is given by

$$\phi = \left(\phi_0 - c_r^p\right) / \left(1 - c_r^p\right). \tag{1}$$

This follows from the fact that the rock (as opposed to pore) volume fraction $\mathcal{V}_r$ is given by

$$\mathcal{V}_r = (1 - \phi) = (1 - \phi)\, c_r^r + (1 - \phi)\, c_r^p = 1 - \phi_0 + (1 - \phi)\, c_r^p, \tag{2}$$

where we note

$$c_w^w + c_w^p = 1, \quad c_r^r + c_r^p = 1. \tag{3}$$

If we consider that the elements are incompressible, and if particle dispersion within the water phase is neglected, then the mass conservation of every element in each phase is expressed by (4):

$$\begin{cases} \frac{\partial}{\partial t}\left(\phi c_w^w\right) + \operatorname{div}\left(c_w^w V_w\right) = 0 \\ \frac{\partial}{\partial t}\left(\phi c_w^p\right) + \operatorname{div}\left(c_w^p V_w\right) = T_{rw}^p \\ \frac{\partial}{\partial t}\left((1-\phi) c_r^p\right) = T_{wr}^p \\ \frac{\partial}{\partial t}\left((1-\phi) c_r^r\right) = 0. \end{cases} \tag{4}$$

T_{wr}^p is the rate of transfer of particles between the water phase and the rock phase, which has a negative sign for transfer from the rock phase to the water phase. Volume conservation of the exchanged particles implies

$$T_{wr}^p = -T_{rw}^p. \tag{5}$$

V_w is the Darcy velocity (6) of the water phase:

$$V_w = -\frac{K}{\mu_w} \frac{\partial}{\partial x} p. \tag{6}$$

The rock absolute permeability is K, which is a function of ϕ. This $K - \phi$ relationship is important since we expect the particle entrapment to reduce the effective permeability of the rock. The water dynamic viscosity is μ_w, and the fluid pressure is p. Note that gravity effects are neglected too since the problem is dominated by pressure gradient effects. We choose the following initial conditions for inflow:

$$c_w^p(0,x) = 0 = c_r^p(0,x) \tag{7}$$

and the following inflow boundary conditions

$$c_w^p(t,0) = c_i, \quad p(t,0) = p_i, \quad p(t,L) = p_o. \tag{8}$$

Although the equations are easier to solve in 1 dimension when the flow rate is fixed at the inlet, this situation is not representative of the experimental conditions for inflow filtration, where we rather fix the inlet and outlet pressures.

The backflow experiments—and therefore also our simulations—are normally performed at constant flow rate. For backflow, the initial condition will be the result of the filtration problem. In general, the total volume of particles is conserved at any point in the porous medium at the instant of switching from injection to backflow:

$$(1-\phi)\, c_r^p(0,x)_{\text{back}} + \phi c_w^p(0,x)_{\text{back}} = (1-\phi)\, c_r^p(T_f,x)_{\text{in}} + \phi c_w^p(T_f,x)_{\text{in}}, \tag{9}$$

where T_f is the duration of the inflow filtration process, and we reset t to zero at the start of backflow. We consider two options for the backflow initial conditions. In the first case, all particles that were trapped after inflow remain trapped when the flow is reversed:

$$\begin{cases} c_w^p(0,x)_{\text{back}} = c_w^p(T_f,x)_{\text{in}} \\ c_r^p(0,x)_{\text{back}} = c_r^p(T_f,x)_{\text{in}}. \end{cases} \tag{10}$$

In the second case, we assume that all particles are released when the flow is reversed:

$$\begin{cases} c_r^p(0,x)_{\text{back}} = 0 \\ c_w^p(0,x)_{\text{back}} = c_w^p(T_f,x)_{\text{in}} + \frac{(1-\phi)}{\phi} c_r^p(T_f,x)_{\text{in}}. \end{cases} \tag{11}$$

This assumption is justified when we consider that geometrical entrapment is due to viscous drag on the particles, which will vanish if the flow rate is zero. In addition, it is assumed that all particles are released when the flow is reversed. Then, the question arises whether this release occurs instantaneously. We point out that this assumption is valid (1) if the friction between particles is negligible and (2) if the particles are not elastic solids. It is believed that the forces holding the particles together are small (Stokes drag due to flow around each particle) and that, as a consequence, friction between the particles is small. Therefore, by stopping the flow, it is expected that the particles would instantaneously settle in the pore in which they are located and that, by reversing the flow, they are allowed to move again since the force that held them trapped has disappeared. If friction was significant, the reversing of the flow may require a certain threshold before the particles are released. This situation is not considered here.

Apart from particle entrapment, we will also consider *erosion* of trapped particles during backflow as a function of the drag force exerted by the fluid. This will be explained in more detail in Sect. 6. We choose the following boundary conditions for backflow:

$$c_w^p(t,L) = 0, \;\; V_w(t,L) = V_w^{\text{back}}. \tag{12}$$

Recombining (4), we see that

$$\begin{cases} \operatorname{div}(V_w) = 0 \quad \textit{i.e.} \text{ in 1D:} \quad V_w = V_w(t) \\ \frac{\partial}{\partial t}\phi = T_{rw}^p \\ \frac{\partial}{\partial t}(\phi c_w^p) + \operatorname{div}(c_w^p V_w) = T_{rw}^p. \end{cases} \tag{13}$$

Equation (13) features one linear hyperbolic equation for ϕc_w^p coupled with a non-linear source term, which is itself a function of ϕ and ϕc_w^p, plus a non-linear differential equation

for ϕ, plus an elliptic equation for the pressure once Darcy's law is used. Following the idea of introducing a new conservative variable as in Tardy and Quintard (1999), we note:

$$u = \phi c_w^p. \tag{14}$$

Using an expression for the rate of entrapment T_{rw}^p, which will be defined in Eqs. (18) and (20), we have

$$\begin{cases} \operatorname{div}(V_w) = -\frac{1}{\mu_w}\frac{\partial}{\partial x}\left(K(\phi)\frac{\partial}{\partial x}p\right) = 0 \\ \frac{\partial}{\partial t}\phi = -\lambda V_w(p,\phi)\frac{u}{\phi}\left(1 + b(\phi_0 - \phi)\right) \\ \frac{\partial}{\partial t}u + \operatorname{div}(\frac{u}{\phi}V_w(p,\phi)) = -\lambda V_w(p,\phi)\frac{u}{\phi}\left(1 + b(\phi_0 - \phi)\right). \end{cases} \tag{15}$$

Equation (15) is the final form of the flow equations that we will solve using numerical tools.

To close the problem, we need to specify phenomenological relationships for the rate of entrapment T_{rw}^p, and the permeability K, as a function of porosity. One possible choice to model the dependence of K on ϕ is to use the Kozeny–Carman equation:

$$K(\phi) = a\frac{\phi^3}{(1-\phi)^2} \tag{16}$$

where a is a positive parameter. Another possibility is to use the following model

$$K(\phi) = K_0\left(1 - \frac{\phi_0 - \phi}{\phi_0}\right)^n, \tag{17}$$

which yields a steeper decrease in the permeability for $n \geq 3$ than the Carman–Kozeny model.

2.1 Entrapment Kinetics

The rate of entrapment is defined, as in Fordham et al. (1991):

$$T_{rw}^p = -\lambda V_w c_w^p F(\phi), \tag{18}$$

where λ is the filter coefficient (in units of reciprocal length). The function $F(\phi)$ accounts for the fact that the trapping rate increases as the filter becomes increasingly clogged. We use[1]

$$F(\phi) = 1 + b(\phi_0 - \phi). \tag{20}$$

No information was available on the numerical value of b. In Fordham et al. (1991), b was taken as 0, while in other cases, b was taken as 1. Equation (18) postulates that the entrapment rate of one particle is proportional to its velocity. The rate of entrapment in time, which is what T_{rw}^p represents, is proportional to the number of pore throats (or other trapping sites) encountered by the particle, per unit time. The faster it moves, the more potential trapping sites it encounters in each unit time interval, and hence the more likely it is to be trapped during that interval. Also, the rate of entrapment of the particles is proportional to their volume concentration in the fluid. These two assumptions are reasonably intuitive.

[1] This is a Taylor expansion of a more general form and is sensible for $|\phi_0 - \phi| \ll 1$. Now, in reality $F(\phi) \uparrow \infty$ as $\phi \downarrow 0$, so to capture the behaviour of complete clogging, we would need a non-linear function like

$$F(\phi) = 1 + b'\frac{\phi_0 - \phi}{(\phi/\phi_0)^n}. \tag{19}$$

The main question is how to interpret the filter coefficient λ. λ is related to the probability of a particle being trapped at each encounter it has with a pore. To see this, consider a situation where a rock contains a spatially uniform concentration of free particles at time $t = 0$. The flow is started, and we look at what happens after a time δt. A slice of thickness δx and cross-sectional area A will have moved after δt over a distance $V_w \delta t/\phi$, where V_w is the Darcy fluid velocity. Moving with the slice under consideration, the number of particles trapped N_t is then

$$N_t = \frac{A\delta x \lambda V_w c_w^p F(\phi)\delta t}{\frac{4}{3}\pi r_p^3}, \tag{21}$$

where r_p is the radius of a particle. The initial number of particles in the slice N_i was

$$N_i = \frac{\phi A \delta x c_w^p}{\frac{4}{3}\pi r_p^3}. \tag{22}$$

The number of pores traversed by the slice is $(V_w \delta t/\phi)\,/\,l_p$, where l_p is a typical pore size. The fraction of particles trapped, divided by the number of pores encountered, is an estimate of the probability of a particle being trapped at each pore it encounters. It follows that this probability is equal to

$$P_{\text{trap}} = \frac{N_t}{N_i} = \lambda l_p F(\phi). \tag{23}$$

Now, if $\lambda l_p \sim \mathcal{O}(1)$, particles have a high chance of being trapped at each pore encounter. If $1/\lambda \gg l_p$, particles have a small chance of being trapped at each pore encounter and penetrate many pore diameters into the rock. For this reason, it may be expected that P_{trap} decreases with decreasing ratio of particle size to pore size $\left(\frac{r_p}{l_p}\right)$.

3 Dimensional Analysis

To identify the factors that control particle trapping, we consider fluid inertia, particle inertia, viscous drag, Brownian motion and sedimentation (Russel et al. 1995). The relative importance of these factors can be estimated by evaluating the following dimensionless numbers: Reynolds number Re, Stokes number St, Peclet number Pe and sedimentation number N_G.

The relevant length scales in this case are the average pore diameter l_p and the particle radius r_p. Note that pores (in sandstones) are generally not equidimensional; one would expect (1) a 'channel' dimension l_c along the extended direction of the pore, associated with the diameter of a rock grain particle, and (2) a smaller dimension l_t perpendicular to the previous one, associated with the pore throat. As there are no numbers available for l_t and l_c, we will not elaborate this and use the average pore diameter l_p. The time scale of interest for flow is $l_p/\langle v\rangle$, where $\langle v\rangle = \frac{V_w}{\phi}$ is the average pore velocity and V_w is the Darcy velocity. Therefore, the inertial force per unit volume is $\mathcal{O}(\rho \langle v\rangle^2 / l_p)$. The viscous force per unit volume is $\mathcal{O}(\mu \langle v\rangle / l_p^2)$. The ratio between these forces is the Reynolds number Re:

$$Re \equiv \frac{\rho l_p \langle v\rangle}{\mu}. \tag{24}$$

Using our system parameters, as listed in Table 1, we find that the Reynolds number is small $\left(\mathcal{O}\left(10^{-2}\right)\right)$, so that inertial effects in the fluid are negligible.

Table 1 System parameters (from Bailey et al. 2000)

Name	Symbol	Value
Particle radius	r_p	4 μm (for C1) 29 μm (for C3)
Average pore diameter	l_p	33.5 μm
Rock porosity	ϕ	0.17
Darcy fluid velocity	V_w	1.3×10^{-3}m/s
Fluid viscosity	μ	30×10^{-3}Pa s
Fluid density	ρ	1.2×10^3 kg/m^3
Particle density	ρ_p	2.7×10^3kg/m^3
Kinetic energy	$k_B T$	4.1×10^{-21}J

The Stokes number St characterises the importance of the particle inertial force

$$F_{\text{inertia}} = \frac{\langle v \rangle^2}{l_p} \rho_p \frac{4}{3} \pi r_p^3 \tag{25}$$

compared with the Stokes viscous drag forces acting on the particle,

$$F_{\text{Stokes}} = 6\pi \mu r_p \langle v \rangle, \tag{26}$$

as a mechanism for particle trapping:

$$St \equiv \frac{2\rho_p \langle v \rangle r_p^2}{9\mu l_p}. \tag{27}$$

Using our system parameters, we find $St \simeq \mathcal{O}(10^{-4})$, which means that particle inertia does not play a role.

Brownian motion causes particles to randomly move in the vicinity of the rock grain surface, on a Brownian time scale of $\mathcal{O}\left(l_p^2/D_0\right)$, where D_0 is the Stokes–Einstein diffusion coefficient, which equals $k_B T/6\pi r_p \mu$. The ratio of this time scale to the convective time scale $\left(\mathcal{O}(l_p/\langle v \rangle)\right)$ defines the Peclet number:

$$Pe \equiv \frac{6\pi \mu r_p l_p \langle v \rangle}{k_B T}. \tag{28}$$

Using our system parameters, we find $Pe \simeq \mathcal{O}(10^8)$, which implies that Brownian motion is unimportant as a mechanism for particle entrapment.

Similarly, the ratio of the sedimentation force

$$F_G = \Delta\rho g \frac{4}{3} \pi r_p^3 \tag{29}$$

to the viscous drag force (Eq. 26) gives the sedimentation number

$$N_G \equiv \frac{2}{9} \frac{r_p^2 \Delta\rho g}{\mu \langle v \rangle}. \tag{30}$$

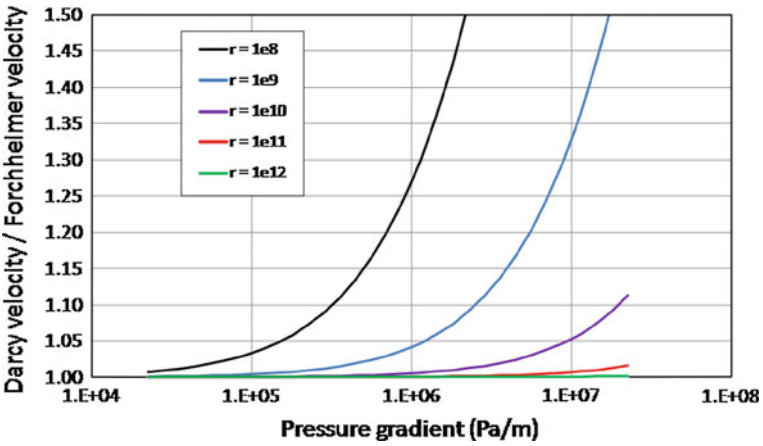

Fig. 3 Ratio of Darcy to Forchheimer velocity as a function of near wellbore pressure gradient for different values of the ratio r of the filtrate viscosity to the matrix permeability

Again, using our system parameters, we find $N_G \simeq \mathcal{O}(10^{-4})$. This implies that sedimentation is unimportant, whereas convection is the dominant mechanism of particle capture.[2]

In the following, we further discuss the importance of inertial forces, on both fluid and particles, compared to viscous forces and the effect of fluid rheology. First, high particle inertia can be achieved locally near the drill bit by the crushing and splitting of the rock. However, such an inertial effect cannot promote particle invasion beyond 1 or 2 pores in the matrix, as the particle would collide very early with a grain making up the matrix of the porous rock. It is our understanding that such inertial effects can be neglected when studying deep bed filtration. High inertia may also be the result of higher flow velocities. If the Stokes number (Eq. 26) is not small, the effect of inertia on the particles could be accounted for by relating the filtration coefficient to the Reynolds number in Eq. 24. When inertia is negligible, the drag force on obstacles is proportional to V as the drag coefficient is inversely proportional to the Reynolds number. Equation 24 is therefore consistent with the use of Darcy's law (Eq. 6) where inertial effects are neglected. The criterion for neglecting inertial effects is given by the Stokes number (Eq. 26).

In the following, we present a discussion on the importance of inertia related to higher flow velocities. Although we will not consider this in the current manuscript, the model presented here could be extended to account for inertial effects by using the Forchheimer equation

$$\frac{\partial}{\partial x} p = \frac{\mu_w U}{K} + \beta \rho_w U^2 \tag{31}$$

where μ_w = filtrate viscosity (Pa.s.), ρ_w = filtrate density (kg/m^3), β = coefficient of inertial resistance (1/m) $\approx 2.43 \times 10^{-6} / K^{1.1045}$ (Dake 2002) and K = matrix permeability (m^2). This equation should be used instead of Darcy's equation (Eq. 6) when high fluid velocities are expected. In the matrix, the importance of inertia depends on the local pressure gradient near the wellbore (Eq. 31). In Fig. 3, we show the ratio of the Darcy velocity to the Forchheimer velocity as a function of the near wellbore pressure gradient for various values of the

[2] Note that the rate of drilling fluid invasion under field conditions is believed to be much smaller than under our laboratory conditions and is estimated to be approximately 3 ft / week (Dussan, personal communication). This results in $N_G \simeq \mathcal{O}(1)$, thus implying that sedimentation might play a role under such conditions.

ratio r of the filtrate viscosity to the matrix permeability, where $r = \frac{\mu_w}{K}$. For a 1 cP filtrate into a 100 mD rock, $r = 1 \times 10^{-10}$. Considering 1cP for the drilling fluid viscosity, the graph shows that a maximum error of 5% is achieved for pressure gradients below 1×10^{-7} Pa/m (440 psi/ft) for rocks up to 100 mD. Since drilling fluids generally have significantly higher viscosity, it is believed that neglecting inertia constitutes a reasonable simplification in many cases. However, if inertia is significant (higher permeability and high pressure gradient), the model should be extended by using the Forchheimer Equation and a drag coefficient which depends on the Reynolds number.

Another refinement to the model is also to account for the non-Newtonian rheology of the drilling fluid and to make the viscosity μ_w a function of the local filtration velocity. Numerous models of apparent viscosity of non-Newtonian fluids in porous media have been proposed in the literature, using an apparent shear rate that depends on flow velocity, permeability and porosity. The likely effect for a shear-thinning fluid would be to reduce the drag forces closer to the wellbore, relative to deeper into the matrix, and this may affect the entrapment mechanism. This effect has not been studied in the current article.

It may be argued that, during drilling, frictional heat generation has a significant effect on the liquid properties. In this respect, we point out that the fluid properties are assumed to be those obtained considering the wellbore temperature, at the depth along the wellbore where the invasion is being considered. Temperature variations in time and space may be expected during drilling operations due to the injection of a cooler fluid, friction caused by the drill bit, Joule–Thomson effect of the drilling fluid jetted through the bit and flowing into the matrix, heat transfer in the wellbore and between fluid and matrix in the pores. These effects may influence the fluid properties, but they have been neglected here as they would require a comprehensive energy balance equation to be accounted for properly. This is beyond the scope of this article. The main assumption here is that the temperature is constant in time in the zone in which the fluid invades, during this invasion, and at the depth along the wellbore under consideration. No assertion is made here of what this temperature should be. The temperature effect may be investigated in the future.

Finally, we note that the water chemistry is assumed not to cause particle release. Otherwise, the equations in the model would need to be modified. The release of particles due to a change in water pH or ionic strength and the subsequent formation damage have been reported in the literature (see for example Stephan 2000).

4 Numerical Model

In the Appendix, we will describe in more detail how a solution of (15) is numerically computed. We outline only the main steps of the resolution in this section.

The discretisation method used is the finite volume technique. This allows us to easily compute the solution of non-linear partial differential equations while keeping the exact balance of every species present in the model. The main difficulties occurring during the resolution of (15) are the non-linearities and the stiffness of the entrapment kinetics (large values of λ), which could lead to numerical instabilities.

The finite volume technique can be understood as a mass balance formulation over an arbitrary volume such as a mesh cell. As a consequence, the fluxes across the faces of the cell have to be determined, and this is done by solving a Riemann problem using the theory of hyperbolic equations. This theory explains how the flux at each interface is a function of the value of the unknown in the two cells around the interface. Actually, it is possible to show

that the flux is constant for a certain period of time δt. So, the system can be solved over such small time steps. These small time steps are also those that provide stability for the numerical solution. In order to simulate over a longer period of time, the solution is averaged over each cell, after each small time increment. Then, a new Riemann problem has to be solved after each increment and so on.

Following the method outlined in Tardy and Quintard (1999), we first split the transport-like terms in the equations from the reaction-like terms modelling the entrapment:

$$\begin{cases} \frac{\partial}{\partial x}\left(K(\phi)\frac{\partial}{\partial x}p\right) = 0 \\ \frac{\partial}{\partial t}u + \operatorname{div}(\frac{u}{\phi}V_w(p,\phi)) = 0 \\ \frac{\partial}{\partial t}\phi = 0 \end{cases} \tag{32}$$

$$\begin{cases} \frac{\partial}{\partial t}u = \frac{\partial}{\partial t}\phi \\ \frac{\partial}{\partial t}\phi = -\lambda V_w(p,\phi)\frac{u}{\phi}\left(1 + b(\phi_0 - \phi)\right). \end{cases} \tag{33}$$

In the same time step, we first solve numerically (32), and we use the numerical solution of (32) as initial data for (33) which we then solve, and so on. (32) is solved using a time-implicit scheme for the pressure and a time-explicit scheme for the porosity ϕ and u. The first pressure equation can then be solved independently from the others. The pressure is determined by inversion of a linear system. The fluid velocity is then calculated with this new pressure (porosity unchanged), and its value is used to solve the linear hyperbolic equation for u. This hyperbolic equation is solved with an upstream explicit finite volume scheme. The pressure p and the intermediate solution of u provide the initial data for (33). Equation (33) is solved by numerical integration of a non-linear partial differential equation. Only the final value of u is to be determined during this step. A backward-Euler scheme is used to cope with the stiffness of the equation (large values of λ) and to allow us to use large time steps. The size of the time step is governed by stability criteria for the resolution of the linear hyperbolic equation for u. Whatever the size of λ, the backward-Euler scheme provides stability with such time steps.

5 Invasion Modelling

In order to validate our deep bed filtration model, the results are compared with experimental invasion data in rock cores. These experimental data consist of synchrotron energy-dispersive X-ray diffraction tomography (EDD-T) and scanning electron microscopy—energy-dispersive spectroscopy (SEM-EDS) profiling data, which are presented in reference (Bailey et al. 1999). The SEM-EDS data, included with kind permission of Statoil R&D, were collected from electron beam line scans of the internal surface of a carefully fractured invaded rock core, see Fig. 4. The synchrotron X-ray EDD-T measurements on the other hand were taken on the intact core, and data were collected from a well-defined volume element at the intersection of the direct beam and the diffracted beam (see Fig. 5). The techniques used are described in more detail in reference (Bailey et al. 1999).

As input for our simulation model, we used the experimental conditions of the core flood filtration tests, as outlined in Bailey et al. (1999). The cores had dimensions $(l \times d)30 \times 25.4$ mm. The porosity was estimated to be 17%, and the initial permeability was 600 mD. The viscosity of the invading fluid was measured to be 30 mPa s, with a solids concentration of 13 % by volume. The inflow filtration was conducted under 300 psi differential pressure (Bailey et al. 1999), corresponding with a Darcy velocity of 1.3×10^{-3} m/s, if we assume that there is no

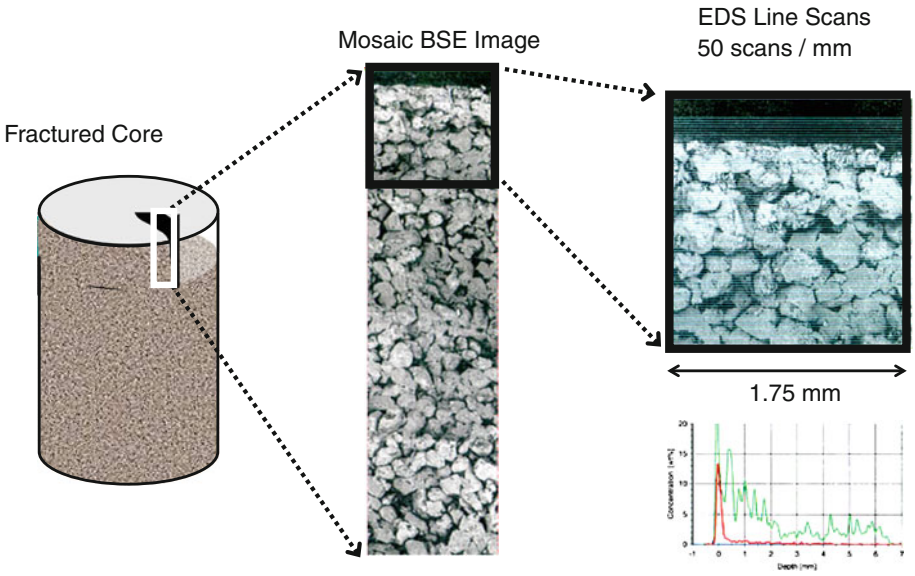

Fig. 4 SEM-EDS analysis of solids invasion

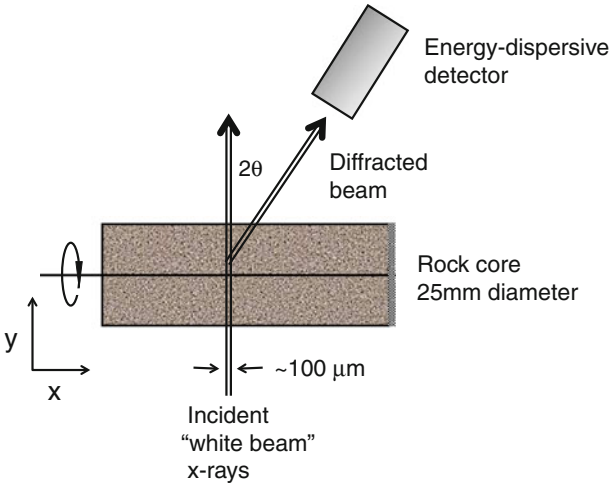

Fig. 5 Synchrotron EDD-T configuration

particle entrapment. The first 10 mm of the core is divided into 1000 grid cells to ensure a high resolution of data points near the core surface to study shallow solids invasion.

Figure 6 compares the simulation results for the trapped solids volume fraction as a function of invasion distance into the core, for values of the filter coefficient λ varying between 10^3 and $10^5 m^{-1}$, with the experimental invasion profiles of calcium carbonates C1 and C3 before backflow. C1 and C3 have a particle d_{50} of 4 and 29 μm, respectively, whereas the Clashach rock core has a pore d_{50} of 33.5 μm, see Table 1. The red curves marked with crosses and pluses represent the results obtained from the different SEM and EDD-T experimental techniques, respectively. The excellent agreement between the two curves lends significant

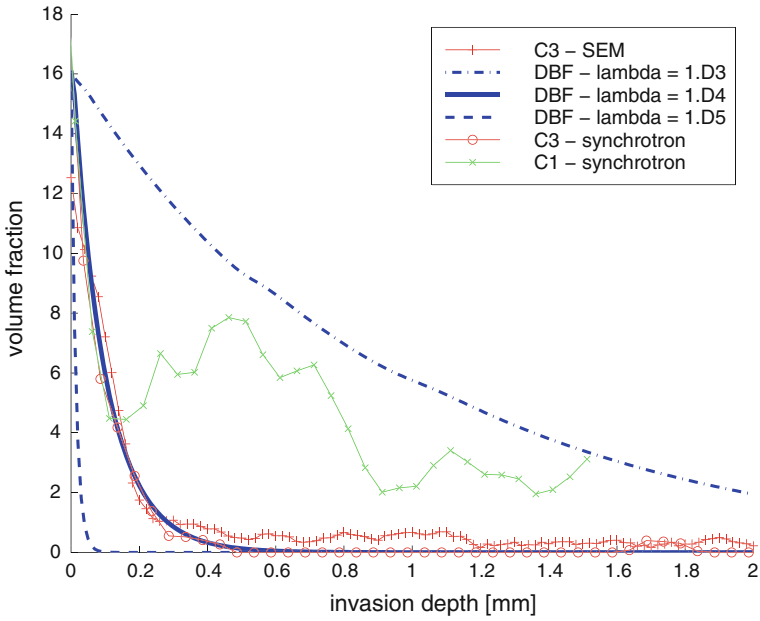

Fig. 6 Comparison of synchrotron EDD-T and SEM-EDS analysis and DBF model profiling of solids invasion. The SEM-EDS data are included with permission of Statoil R&D

credibility to the correctness of the actual measurements. It appears that the experimental invasion curves can be described by values of λ varying between 10^3 and $10^5 \mathrm{m}^{-1}$. In particular, the profiles for carbonate C3 can be fitted very well to a simulated profile with $\lambda = 10^4 \mathrm{m}^{-1}$.

As already mentioned, the filter coefficient λ can be considered as a function of two characteristic lengths: the size of the invading particle and the pore size. For this reason, we expect λ to have a high value $\approx O$ (pore size $^{-1}$). In more detail, we find that $\lambda l_p \simeq 0.3$, which means that particles are very likely to get trapped during the first couple of pore encounters (see Eq. 23).

In these simulations, we used the permeability–porosity relationship as defined in Eq. (17) with $n = 3$, and the clogging function $F(\phi)$ (Eq. (20)) with b arbitrarily fixed at $b = 1$. As a consequence, λ was the only fitting parameter used to reproduce the experimental data. A series of simulations were performed to check the validity of this approach. First, we studied the role of the value of the parameter n in the permeability function (17), by varying n from 1,5,7 to 9, while λ and b were kept constant at values of $10^4 \mathrm{m}^{-1}$ and 1, respectively. The resulting invasion profiles after a simulation of 1 s, presented as the red curves in Fig. 7, show that the value of n influences the actual profile only very slightly. Second, the role of the parameter b was studied by varying b from 0 to 1,000 while keeping the values of n and λ fixed at values of 3 and $10^4 \mathrm{m}^{-1}$, respectively. The resulting profiles, presented as the green curves in Fig. 7, show that the invasion profile decays faster with increasing value of b. This is in agreement with the faster decay of the invasion profiles for values of λ increasing from 10^3 to $10^5 \mathrm{m}^{-1}$ while keeping n and b constant at 3 and 1, respectively, displayed as the blue curves in Fig. 7. In Fig. 8, the calculated volume fraction of trapped particles is presented as a function of $\lambda(1 + b\phi_0)$, at a distance along the core arbitrarily fixed at 0.2 mm. This figure shows that, for values of b varying from 0, 0.1, 1 to 10, all simulated data for constant values

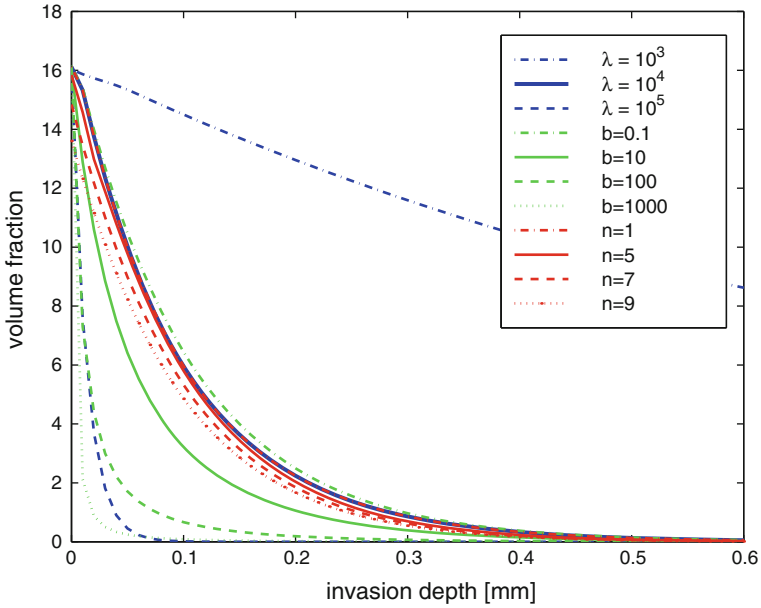

Fig. 7 Invasion profiles as a function of λ (*blue*), *b* (*green*) and *n* (*red*)

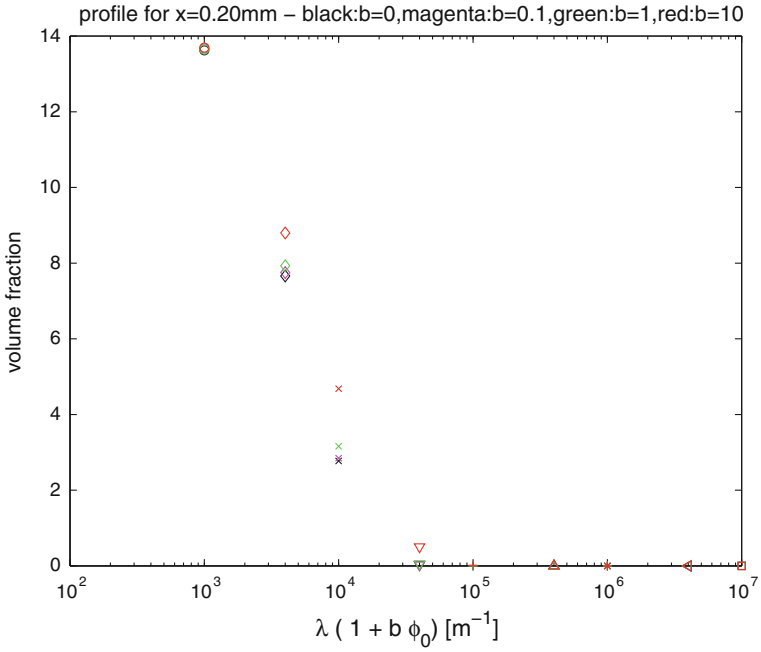

Fig. 8 Volume fraction of trapped particles at a distance of 0.2 mm along the core, for values of *b* fixed at 0 (*black*), 0.1 (*magenta*), 1 (*green*) and 10 (*red*)

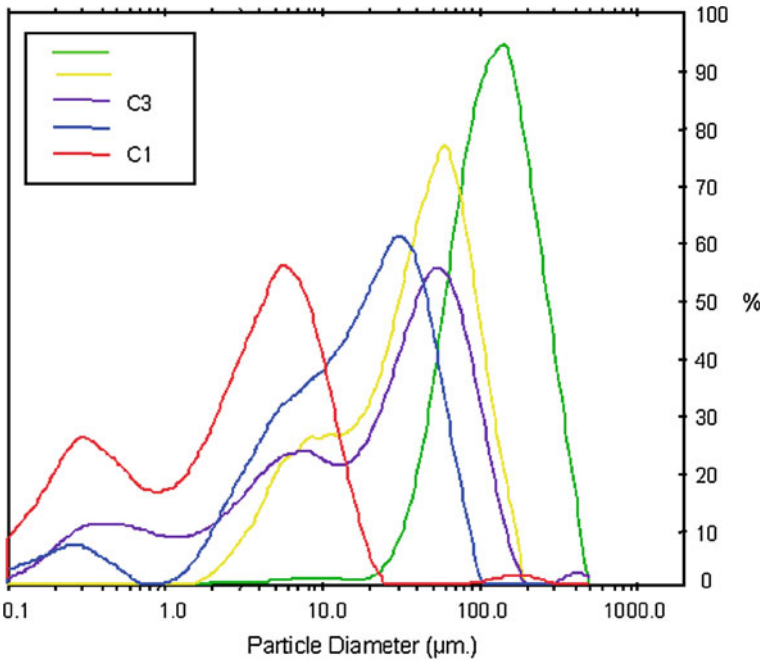

Fig. 9 Particle size distributions for carbonates C1 and C3, as determined by light scattering measurents (Francis 1997)

of $\lambda\,(1 + b\phi_0)$ almost collapse on a single curve, for $b \leq 1$. The match is particularly good for $\lambda\,(1 + b\phi_0) > 10^5$ and for $\lambda\,(1 + b\phi_0) = 10^4$. In other words, the trapping function T^p_{rw} (Eq. (18) scales as $\lambda' = \lambda\,(1 + b\phi_0)$ as long as $b \leq 1$. In the following, we fix b to 1, and therefore, λ is the only important fitting parameter in the problem.

The invasion profile of carbonate C1 follows the DBF profile with $\lambda = 10^4 \mathrm{m}^{-1}$ quite closely up to 0.2 mm, but with increasing invasion depth, the experimentally observed invasion exceeds the model prediction. This may be due to the particle size distribution of carbonate C1. It appears that this carbonate has a bimodal distribution, with peaks around 6 and 0.3 µm, see Fig. 9. It may be that the bigger particles cause the observed clogging at the inlet of the core (and play a major role in the formation of external filter cake). The smaller particles on the other hand may be able to penetrate much farther. This implies that the trapping probability $P_{\mathrm{trap}} \ll 1$ (Eq. 23) and therefore $\lambda \ll 1/l_p$. Fitting this behaviour would require modification of the model to incorporate two (or more) particle-trapping coefficients, as well as supplementary evolution equations and c^p_w/c^p_r variables. We note that modelling the contribution of polymer in filtrate would also require a polymer trapping coefficient and mass conservation equations to be added to the model.

During inflow filtration, the porosity of the rock will decrease as a consequence of particle entrapment. However, we allow the porosity to decrease only to a minimum value ϕ_{lim}.[3] The reason for doing this is to avoid numerical instabilities when the actual porosity approaches

[3] Alternatively, in order to have permeability $K = 0$ when trapped solids fill a fraction 1 - ϵ of the original pore space, then one would need

$$K(\phi) = K_0 \left(1 - \frac{\phi_0 - \phi}{(1-\epsilon)\,\phi_0}\right)^n, \tag{34}$$

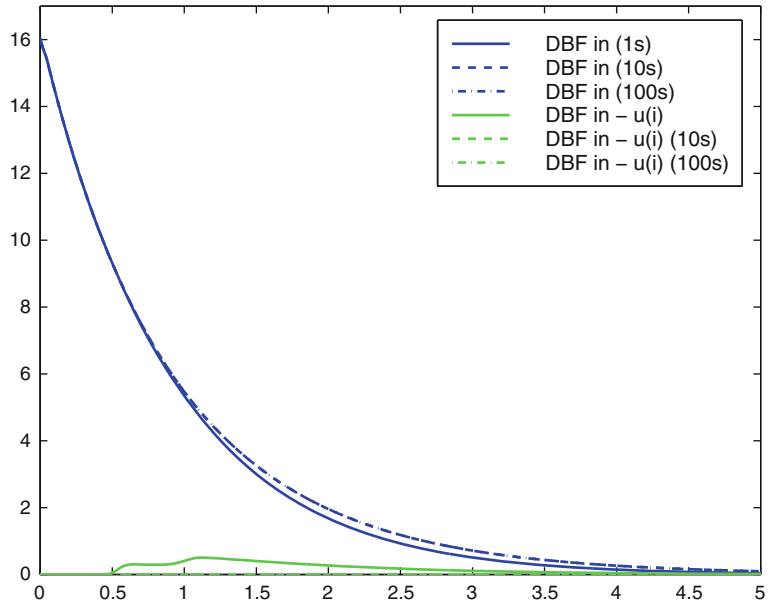

Fig. 10 Comparison of invasion times of 1s, 10 and 100s. The *blue* trapped particle profiles indicate that the effects saturate after 10 s. The *green curves*, indicating the concentration of untrapped particles, indicate that all invaded particles are essentially trapped after 10 s

zero. Indeed, if the porosity goes to zero, then the flow Eqs. (15) degenerate (all terms go to zero) and *e.g.* c_w^p is not defined anymore. In that case, any numerical model will fail to determine c_w^p.

Physically, limiting the porosity decrease is required when we consider that the available pore space will only allow a maximum concentration of particles to be trapped, corresponding with the packing volume fraction (PVF) of solid particles. For monodisperse spherical particles, the PVF is roughly 0.6, but this may readily approach 0.9 with increasing particle polydispersity. In our case, we will use $\phi_{\lim} = 0.01$, which seems reasonable in view of a highly impermeable internal filtercake. When the porosity approaches $\phi_{\lim}$, effectively an external filter cake will start to build up, which will prevent inflow of particles into the rock. In our case, the particle flux ($c_w^p V_w$) is set to zero when $\phi \leq \phi_{\lim}$, but water can still flow free of particles at this point. Although it would be straightforward to extend the current model to account for the build-up of an external filter cake (using mass balance considerations), this is outside the scope of the current paper.

In this section, we will discuss the effect of total simulation time on the results. The results described above are obtained over a simulation time of 1 s. Profiles computed over 10 s show marginally deeper invasion than those computed over 1 s. It appears that increasing the simulation time to 100 s does not change the results, as the curves are already saturated after 10 s. The results of these simulations are shown in Fig. 10. This indicates that the invasion process takes place over a short time scale and can probably be associated with the spurt phase seen in experiments.

Now, we turn to spurt loss. If we define the fraction of trapped particles (with respect to the total volume of particles) as $\sigma = c_r^p(1-\phi)$, then we can say that the total volume of solids trapped in the rock core, with entrance surface area A, at the end of spurt loss is equal to

although this has not been further pursued in the current work.

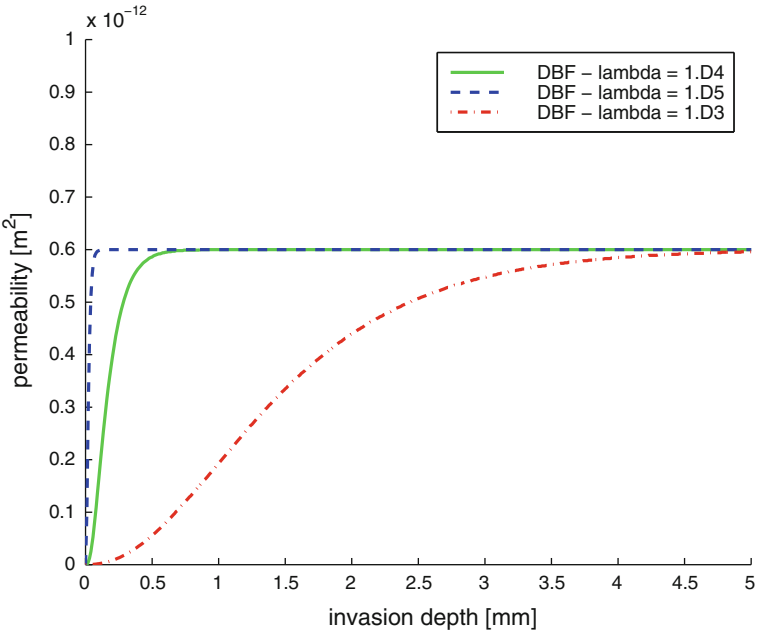

Fig. 11 Permeability profiles predicted for values of the filter coefficient λ varying between 10^3 and 10^5 m^{-1}

$$A\int_0^L \sigma \,\mathrm{d}x = \frac{\frac{1}{2}\phi_0 A}{\lambda} \tag{35}$$

if we assume that all solids are trapped, and $\sigma \simeq \frac{1}{2}\phi_0 \exp(-\lambda x)$. The factor $\frac{1}{2}$ is included here to account for the fact that the packed particles have a finite porosity. We choose this functional form because it is the long time solution when the governing equations are linearised:

$$\begin{cases} \phi \frac{\partial}{\partial t} c_w^p + V_w \frac{\partial}{\partial x} c_w^p = -\lambda c_w^p V_w \\ (1-\phi) \frac{\partial}{\partial t} c_r^p = \lambda c_w^p V_w. \end{cases} \tag{36}$$

The assumptions in this linearised model are that σ is small, so the rock porosity is taken constant ($\phi = \phi_0$), and the clogging factor $F(\sigma)$ is taken equal to 1.

Although the above assumptions may not be entirely justified in the case under consideration, one can imagine that the functional form is intuitively correct.

The volume of trapped solids in turn is equal to $Q_{\text{spurt}} c_{\text{mud}}^{\text{blocking}}$, where $c_{\text{mud}}^{\text{blocking}}$ is the volume fraction in the mud of particles that contribute to the blocking of the core. For carbonate C3, we estimate the experimental spurt loss $Q_{\text{spurt}} \approx 0.1$ml. The spurt loss calculated from DBF simulations with $\lambda = 10^4 \text{m}^{-1}$ is consistent with this figure. Using these values for λ and Q_{spurt}, $c_{\text{mud}}^{\text{blocking}} \simeq 0.15$. This value is roughly equal to the volume fraction of the carbonate particles in the mud (0.13) and implies that all solid particles in the suspension contribute to the clogging process.

The model allows us to convert the invasion profile into a permeability profile and estimate levels of damage to the core. Figure 11 shows the permeability profiles as a function of λ, which mirror the invasion profiles and are dominated by the near-surface clogging.

Table 2 Average permeability of the whole core and the clog for different values of λ before backflow

$\lambda(\mathrm{m}^{-1})$	k_{av} (mD (%))	k_{clog} (mD (%))
10^3	27.6 (4.6%)	1.5 (0.3%)
10^4	63.3 (10.6%)	3.5 (0.6%)
10^5	91.4 (15.2%)	5.3 (0.9%)

A measure of the average permeability k_{av} can be obtained by summing k_i for each grid cell over the length of the core L:

$$\frac{L}{k_{av}} = \sum_i \frac{l_i}{k_i}. \tag{37}$$

The values for the whole core and the clog (first 0.5 mm) are listed in Table 2. From this table, we can see that, in the case of $\lambda = 10^3 \mathrm{m}^{-1}$, the effective average permeability is reduced to $\approx 4.6\%$ of the initial rock permeability. Note that this is the permeability of the invaded core undisturbed by backflow. As the near-surface clogging is responsible for the greatest reduction in permeability, (≈ 1.5 mD to 0.5 mm depth, rather similar to that calculated by Francis (1997) and reasonable for filtercake permeability), we expect a true return permeability to be significantly higher. In the next section, we will discuss the effect of backflow on trapped particle profiles and retained permeability.

6 Backflow Modelling

In the experimental procedure, the damaged rock cores are subject to backflow with brine or kerosene, in order to measure the retained permeability. The idea is that backflow will partially clean up the internal damage—a recent study (Bailey et al. 1999) claims that $\approx 30\%$ of the near-surface invaded material is removed. It is the aim of this study to investigate this in some detail. In order to simulate this, we need to consider continued trapping, as well as release of particles during backflow. The backflow experiments (and therefore our simulations) are normally done at constant flow rate rather than constant pressure difference across the core. In our simulations, we impose a constant Darcy velocity V_w of 3.3×10^{-4}m/s. This corresponds with a volumetric flow rate Q of 10 ml/min, which is a usual value for backflow filtration experiments (Bailey et al. 1998). The constant flow rate simulations enable us to to measure the flow initiation pressure (FIP), which is the observed pressure peak during backflow, believed to be associated with rupture of the filtercake (Bailey et al. 1999, 2000). It has been shown that relative permeability effects can also contribute significantly to the FIP (Ladva et al. 2000). Note that we only consider single-phase inflow and backflow, and therefore, relative permeability effects are excluded. The second goal of this study is to investigate to what extent internal damage contributes to the FIP.

During the backflow simulations, the flow is reversed (in practice, this is achieved by reversing the grid cells rather than the direction of the flow). We assume that the inlet concentration of particulates in the backflow fluid phase is zero, *i.e.* $c_w^p(t, 0) = 0$. Two extreme scenarios are considered initially:

1. all particles that were trapped during inflow filtration remain trapped, and trapping continues during backflow

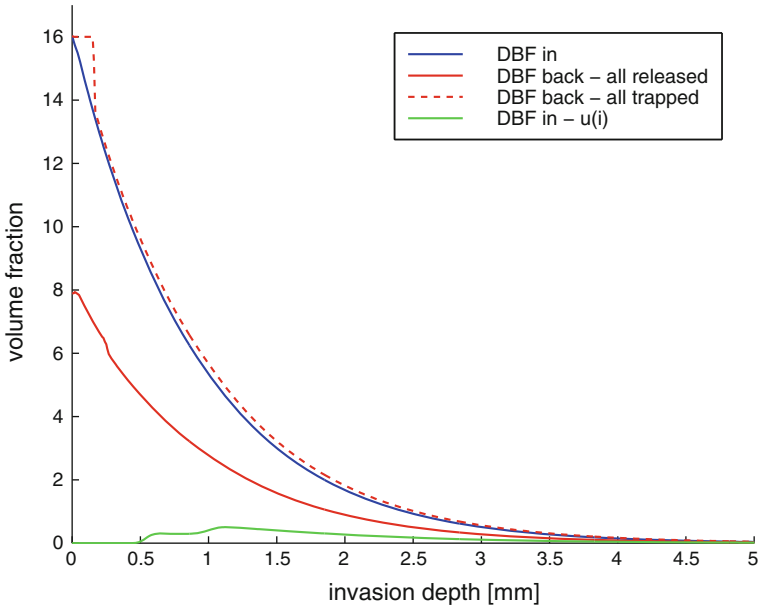

Fig. 12 DBF model profiling of solids invasion, for $\lambda = 10^3 \mathrm{m}^{-1}$. The trapped particle profile before backflow is drawn in *blue*, the *red* drawn profile represents the profile after backflow where all captured particles were released, the *red dashed curve* indicates backflow where all captured particles remain captured. The *green* profile is the concentration of untrapped particles before backflow

2. all trapped particles get *released* when the flow rate is reversed, and trapping starts afresh during backflow

The entrapment kinetics used during backflow are the same as for inflow (Eq. 18).

Upon backflow, we observed in initial calculations that, in the case where all particles remain trapped, the concentration of trapped particles in the clog still exceeded ϕ_{lim} (as defined in the previous section). Clearly, this is is an undesired effect. This problem can be solved by realising that pores contain both trapped *and* untrapped particles. Therefore, we require that if $\phi - u \leq \phi_{\mathrm{lim}}$, then the particle flux will be set to zero. The simulations were carried out using the same rock properties as those used during inflow filtration. This results in invasion / backflow profiles as shown in Fig. 12. This figure shows that backflow without releasing any trapped particles at the start of backflow generates an internal filtercake clog of uniform concentration ($\phi_0 - \phi_{\mathrm{lim}}$). Removal of invaded particles by backflow can be quantified by integrating the concentrations of trapped particles over the length of the core. The results are listed in Table 3. We find that, when all particles are released and retrapping starts upon backflow, 48% of the invaded particles are removed from the core (49% if only the first 0.5 mm is considered). When all particles remain trapped upon backflow, all the untrapped particles get trapped upon backflow, and no particle will escape from the core. The total amount of shallow invasion is then 6% higher compared to the situation before backflow. Experimentally, it is found that backflow removes roughly 30%. This percentage is within the limits of our two extreme cases, and therefore, it should be possible to define an untrapping fraction that gives rise to the observed 30% removal.

Figure 13 shows the permeability profiles before and after backflow. The average permeability of the rock samples was calculated according to Eq. 37. The results are shown in

Table 3 Release of particles upon backflow

	% particles released upon backflow	Clog only (%)
All released	48	49
All trapped	−6	−5

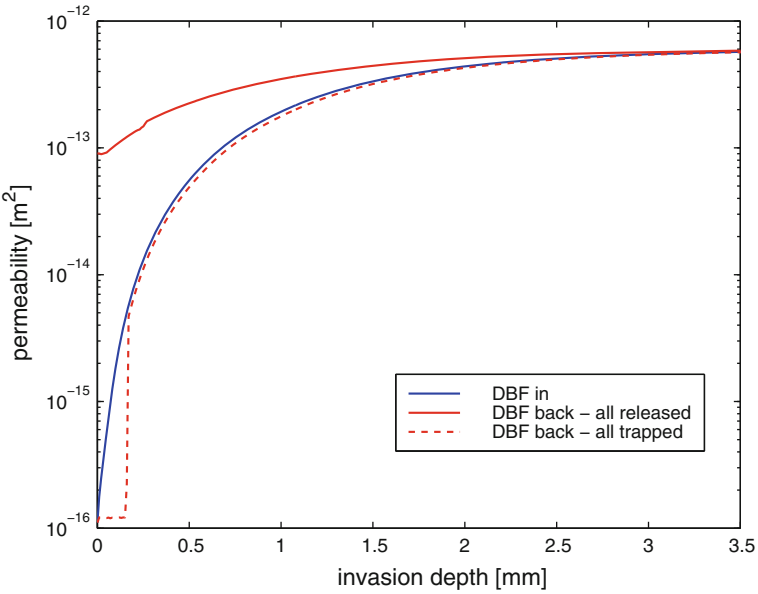

Fig. 13 DBF model profiling of permeability, for $\lambda = 10^3 \mathrm{m}^{-1}$. The permeability profile before backflow is drawn in *blue*, the *red* drawn profile represents backflow where all captured particles were released, the *red dashed curve* indicates backflow where all captured particles remain captured

Table 4 Average permeability of the whole core and the clog after backflow

	k_{av} (mD (%))	k_{clog} (mD (%))
Before backflow	28 (4.6%)	1.5 (0.3%)
All trapped	7 (1.2%)	0.4 (0.1%)
All released	472 (78.7%)	140 (23%)

Table 4. When all particles remain trapped, the retained permeability is only 1% of the initial rock permeability (7 mD). On the other hand, if all particles are initially released, the retained permeability is 79%. If only the surface clog upto 0.5 mm is considered, the results are even more dramatic: the retained perms are only 0.1 and 23%, respectively.

We now turn to the question to what extent the FIP can be explained by internal reservoir damage. It has already been shown that relative permeability effects can significantly contribute in this respect (Ladva et al. 2000). For this purpose, the pressure differential profile in the rock is calculated as a function of time. In Fig. 14, the pressure profile is shown for the inlet and outlet. It appears that the pressure difference increases monotonically as a function of time, and so there is no FIP effect.

In order to generate a pressure drop, it may be necessary to invoke erosion of particles during backflow, in addition to the continued trapping. Intuitively, one would expect that the rate of erosion is proportional to the drag force on the trapped particle, with radius r_p:

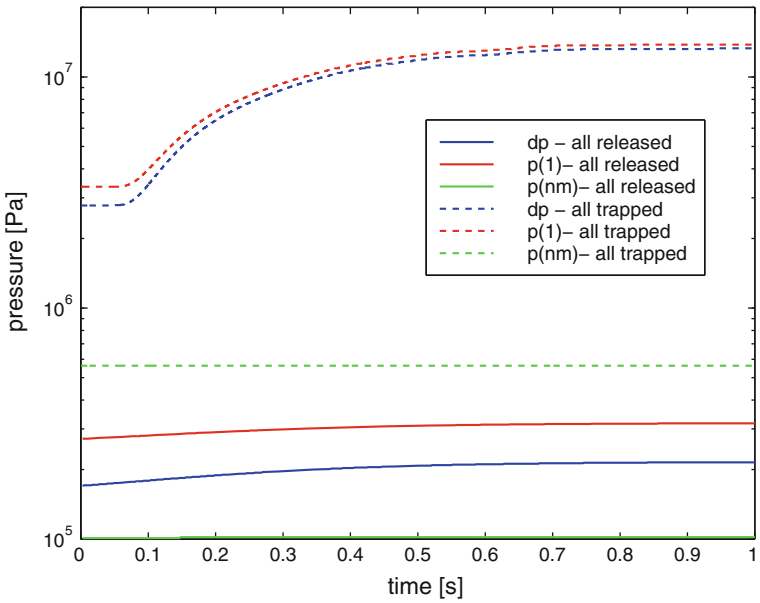

Fig. 14 Pressure profiles for backflow, for case (1) where everything remains trapped (*dashed curves*) and case (2) where everything is released (drawn profiles). The pressure differential over the core is drawn in *blue*, the inlet pressure in *red* and the outlet pressure in *green*

$$F_{\text{Stokes}} = 6\pi\mu r_p \langle v \rangle , \tag{38}$$

where $\langle v \rangle = \frac{V_w}{\phi}$ is the average pore velocity (or frontal fluid velocity) in each grid cell. We postulate a phenomenological rate of erosion, assuming that erosion kicks in as soon as $\langle v \rangle$ exceeds a certain critical value v_{lim}:

$$T^p_{rw} = \lambda'(\langle v \rangle - v_{\text{lim}}) \cdot \mathcal{H}(\langle v \rangle - v_{\text{lim}})\sigma, \tag{39}$$

where $\lambda'(\text{m}^{-1})$ is a rate constant for erosion, $\sigma = \phi - \phi_0$ is the volume fraction of trapped particles, and $\mathcal{H}(\text{x})$ is the Heaviside function which is unity for positive arguments and zero for negative. From the profile of the dimensionless average pore velocity $\frac{\langle v \rangle}{V_w} (= \frac{1}{\phi})$ as a function of invasion depth, as shown in Fig. 15, and Eq. 39, it can be observed that we can increase the level of erosion at the clogged entrance of the core by decreasing the value of $\frac{v_{\text{lim}}}{V_w}$. This is illustrated in Fig. 16. The time required for the erosion process to come to equilibrium decreases with increasing value of the erosion rate constant λ'. For $\lambda' \simeq \mathcal{O}(10^4)$ m^{-1}, the erosion process is equilibrated within a dimensionless time t^* (to be defined in Eq. (40)) of the order of ten pore volumes. Choosing $\frac{v_{\text{lim}}}{V_w} = 8$, we calculate that the percentage of particles removed upon erosion is 35.2%. This shows that the experimentally determined value of 30% removal is within the scope of our simulations.

We will now discuss measurements of the pressure drop along the core as a function of λ'. Simulations were performed at Darcy velocities varying from 3.3×10^{-5} to 3.3×10^{-3} m/s, choosing $\frac{v_{\text{lim}}}{V_w} = 30.3$. When we define a dimensionless time

$$t^* = \frac{t V_w}{L\phi_0} \tag{40}$$

and a dimensionless pressure

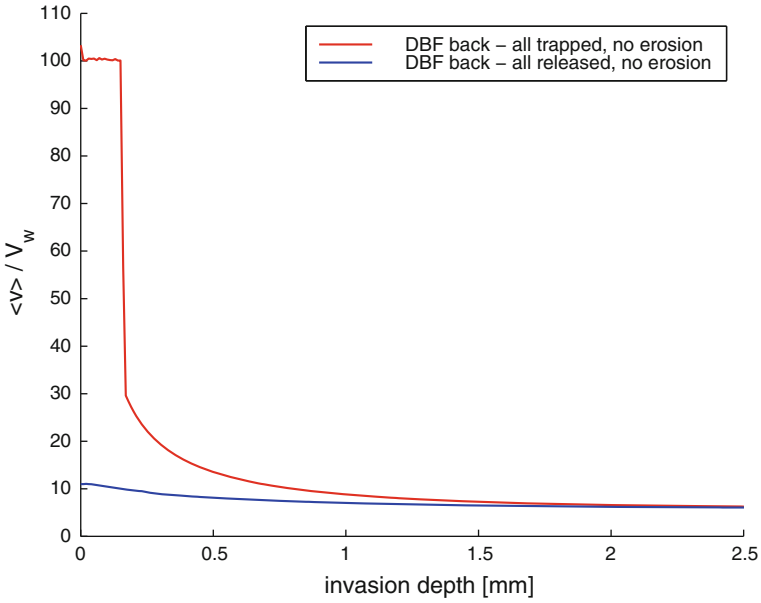

Fig. 15 Dimensionless average pore velocity $\frac{\langle v \rangle}{V_w}$ of the fluid as a function of invasion depth

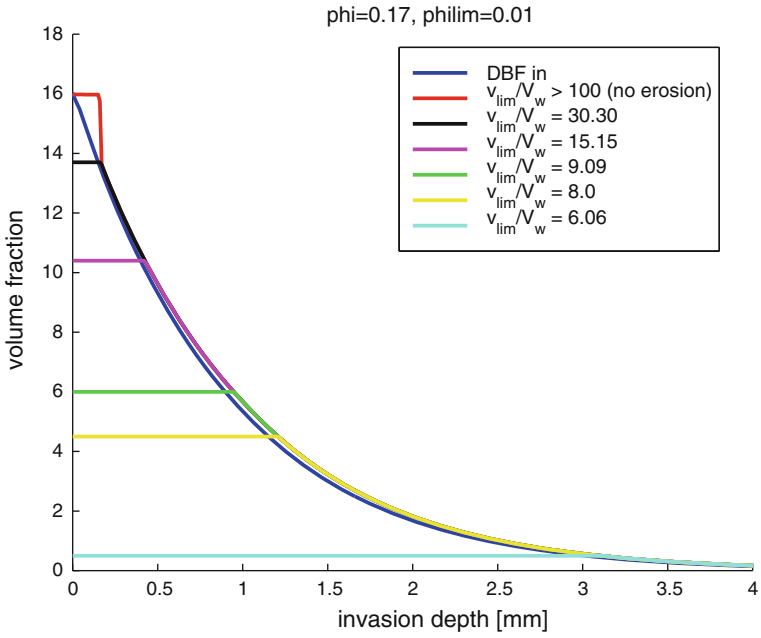

Fig. 16 Maximum level of erosion of trapped particles increases with decreasing value of the dimensionless average pore velocity $\frac{v_{\text{lim}}}{V_w}$, using $\lambda' = 10^4 \text{m}^{-1}$ and $t^* = 10$ pore volumes

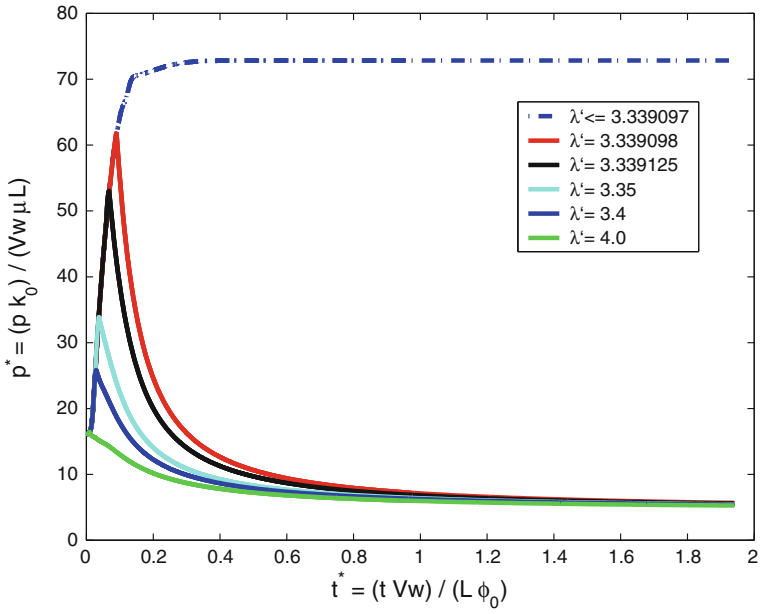

Fig. 17 Pressure profiles for backflow with erosion as a function of number of pore volumes backflushed, for $\frac{v_{\text{lim}}}{V_w} = 30.3$, $\lambda = 10^3$ and λ' varying from 3.3 to 4.0. All particles trapped during inflow filtration remain trapped, and trapping continues during backflow

$$p^* = \frac{pK_0}{V_w \mu_w L}, \tag{41}$$

where ϕ_0 and K_0 are the porosity and permeability of the undamaged rock, respectively, then it appears that, for every single given value of λ', the profiles of p^* as a function of t^* for all Darcy velocities collapse on to a single curve. The results of these simulations are shown in Fig. 17. We find that, when $\lambda' \leq 3.33$, the pressure difference increases monotonically with time, *i.e.* trapping still dominates. For $\lambda' \geq 4.0$ on the other hand, the pressure difference decreases, that is, erosion dominates. In between these two values, there is a region for λ' where the pressure differential first increases as a result of ongoing trapping and then decreases when erosion kicks in. Note that there is a critical value for λ' around 3.339097 m^{-1}.

The dimensionless time t^* is associated with the number of pore volumes that has been backflowed. In our case, it appears that the pressure peak occurs around $t^* = 0.2$ pore volumes. This corresponds, assuming $V_w = 3.3 \times 10^{-4}$m/s, with a real time $t = 0.5$ s.

The dimensionless pressure p^* is associated with the pressure drop due to flow through the damaged core, with the undamaged core before filtration as a reference at $p^* = 1$.

Concluding, we observe a flow initiation pressure (FIP) due to the growth and erosion of an internal filter cake. It should be noted that the region of values of λ' for which this happens is quite small, and therefore, it may be questioned whether it would be easy or likely to observe such behaviour experimentally. Also, the time scale on which the peak in the pressure difference occurs is short compared with the experimentally observed transient time of $\mathcal{O}(10^2)$ s (Ladva et al. 2000). It may be expected that relative permeability effects play a more important role in explaining FIP effects at such a time scale (Ladva et al. 2000). Nevertheless, the jury is out, and the experimentalists are challenged to find a means to

directly observe particles and whether they are trapped or not, as a step towards verifying or refuting the claim above.

7 Discussion

One might argue that one of the reasons why the time scale of our FIP does not correspond with the experimentally observed time scale of the transient time in the pressure as a function of time is the incompressible nature of the fluid in our model. However, it can be shown that the characteristic time τ associated with fluid compressibility is as follows [18]:

$$\tau = \frac{c\phi\mu L^2}{k}, \tag{42}$$

where c is the fluid compressibility (Pa^{-1}) and L the core length. Using the parameters as described before, and choosing $c = c_{\mathrm{water}} = 4.57 \times 10^{-10}\mathrm{Pa}^{-1}$, we find $\tau \simeq \mathcal{O}(10^{-2})$ s. Obviously, the fluid compressibility does not give us the observed transient time of $\mathcal{O}(10^2)$ s. Another possibility could be that the core is not entirely saturated with fluid, but there are still air bubbles left in the core. Considering an air compressibility of $10^{-5}\mathrm{Pa}^{-1}$, we would need a volume fraction of 45.6% air with respect to the total volume occupied by air and fluid. Although there may be some air bubbles present in the core, the fraction required to yield the required transient time is unrealistically high, and we can therefore safely dismiss the possibility of air/fluid compressibility causing the observed transient times.

In principle, the model described in this report could be used to predict the invasion of particulates in a porous medium. This would require further validation of the inflow and backflow filtration model. For this purpose, it would be highly desirable to collect more synchrotron EDD-T data for a variety of particulates and porous media, after both inflow and backflow filtration. Also, it would be desirable to have a better idea of what the λ parameter (Sect. 2.1) actually represents. In fact, λ can be regarded as an upscaled parameter, in which a variety of parameters at the pore level are lumped together.

In the course of this work, we found that the invasion of particulates is actually quite shallow. In the case of carbonate C3, the best part of the invasion is limited to the first 0.4 mm of the core, which is roughly equal to 10 pore spaces (assuming a pore d_{50} of 33.5 μm, see Sect. 5. This implies that it is justified, with hindsight, to ignore hydrodynamic dispersion contributions, as these will only be important at larger length scales. On the other hand, it may be argued that, when the pore channels are not much larger than the particle sizes, a microscopic model is possibly more appropriate than a continuum model. In this case, the pore and particle size distributions become important, and a continuum description may fail. In such cases, an accurate description of particle filtration is only possible by applying discrete particle models that simulate flow and transport in the complicated pore channel network. A discrete particle model describing filtration through three-dimensional granular packings has been reported by Schwartz et al. (1993). There is scope to further develop this type of work, as many-body effects such as buckling, the formation of arches and the importance of hydrodynamic interactions have been ignored. From this point of view, the development of new network models (Rege and Fogler 1988), lattice-Boltzmann (Manz et al. 1999; Boek and Venturoli 2010) dissipative particle dynamics (Boek and van der Schoot 1998) and stochastic rotation dynamics (Boek et al. 2008, 2010a,b) simulation models may be a next step forward.

8 Conclusions

A deep bed filtration model has been developed to quantify the effect of solids invasion on permeability. The calculated particle-trapping profile can be compared quantitatively with experimental profiles from SEM-EDS and EDD-T sources. The computed permeability reduction as a consequence of particle invasion is in broad agreement with experiment. Backflow was modelled by reversing the flow rate, starting off with a situation where all particles either remain trapped or are all released. It appears that the experimentally observed 30% release of particles upon backflow is reproducible within the limits of the two extreme cases. When erosion is included in the model, a peak in the pressure profile is observed. This peak may be correlated with the experimentally observed flow initiation pressure (FIP), which is the backflow pressure needed to initiate flow after initial inflow filtration. Finally, we conclude that internal reservoir damage, within the limits of our 1-D single phase DBF model, may contribute to the experimentally observed flow initiation pressure.

Acknowledgments We are grateful to Olav Selle (Statoil R&D) for granting permission to include the SEM-EDS data, to Louise Bailey, Paul Hammond and Paul Howard for stimulating discussions and to one of the referees for raising questions on inertial effects.

Appendix: Numerical Solution of DBF Model

In Sect. 2, it was shown that the flow continuity equation,

$$\mathrm{div}(V_w) = 0, \tag{43}$$

together with the mass balance equation

$$\frac{\partial}{\partial t}u + \frac{\partial}{\partial x}\left(\frac{u}{\phi}V_w\right) = \frac{\partial}{\partial t}\phi \tag{44}$$

and the kinetic (evolution) equation for the porosity

$$\frac{\partial}{\partial t}\phi = -\lambda V_w \frac{u}{\phi}\left(1 + b\left(\phi_0 - \phi\right)\right) \tag{45}$$

makes up a system of non-linear p.d.e's that must be solved numerically. This system can be further simplified by introducing the following dimensionless independent variables

$$X = \frac{1}{L}x \Rightarrow \frac{\partial}{\partial x} = \frac{1}{L}\frac{\partial}{\partial X}, \tag{46}$$

$$T = \int_0^t \frac{V_w}{L}\mathrm{d}\tau \Rightarrow \frac{\partial}{\partial t} = \frac{V_w}{L}\frac{\partial}{\partial T}, \tag{47}$$

where $V_w > 0$.

The above transformations result in the following system of equations:

$$\begin{cases} \frac{\partial}{\partial X}V_w = 0 \\ \frac{\partial}{\partial T}\phi = -\lambda L\frac{u}{\phi}\left(1 + b\left(\phi_0 - \phi\right)\right) \\ \frac{\partial}{\partial T}u + \frac{\partial}{\partial X}\left(\frac{u}{\phi}\right) = -\lambda L\frac{u}{\phi}\left(1 + b\left(\phi_0 - \phi\right)\right) \end{cases} \tag{48}$$

The method used is to solve (48) is based on an operator splitting as in Tardy and Quintard (1999). The transport terms in the equations are split from the entrapment terms, as follows:

$$\left\{ \frac{\partial}{\partial X}\left(K(\phi)\frac{\partial}{\partial X}p\right)=0 \right. \tag{49}$$

$$\left\{ \begin{array}{l} \frac{\partial}{\partial T}\phi=0 \\ \frac{\partial}{\partial T}u+\frac{\partial}{\partial X}\left(\frac{u}{\phi}\right)=0 \end{array} \right. \tag{50}$$

$$\left\{ \begin{array}{l} \frac{\partial}{\partial T}u=\frac{\partial}{\partial T}\phi \\ \frac{\partial}{\partial T}\phi=-\lambda L\frac{u}{\phi}\left(1+b(\phi_0-\phi)\right) \end{array} \right. \tag{51}$$

where the solution of (50) is used as initial data for (51). Equations 49, 50 and 51 are solved over $X\epsilon[0,1]$, by discretising as follows:

$$[0,1]=\bigcup_{i=1,n_m} M_i, \text{ where } M_i=\left[X_i-\frac{\delta X}{2}, X_i+\frac{\delta X}{2}\right]. \tag{52}$$

We solve (49) by using the finite difference method (for clarity, we note $p(X_i)$ instead of $p(T,X_i)$):

$$\frac{\partial}{\partial X}\left(K(\phi)\frac{\partial}{\partial X}p\right)_{|X=X_i}=\frac{1}{\delta X}\left[\left(K(\phi)\frac{\partial}{\partial X}p\right)_{|X_{i+1/2}}-\left(K(\phi)\frac{\partial}{\partial X}p\right)_{|X_{i-1/2}}\right]+\mathcal{O}\left(\delta X^2\right) \tag{53}$$

$$\left(K(\phi)\frac{\partial}{\partial X}p\right)_{|X_{i+1/2}}=K(\phi)_{|X_{i+1/2}}\left(\frac{p(X_{i+1})-p(X_i)}{\delta X}\right)+\mathcal{O}\left(\delta X^2\right). \tag{54}$$

Then

$$\begin{aligned}\frac{\partial}{\partial X}\left(K(\phi)\frac{\partial}{\partial X}p\right)_{|X=X_i}&=\frac{K(\phi)}{\delta X^2}{}_{|X_{i+1/2}}\,p(X_{i+1})-\left(\frac{K(\phi)_{|X_{i+1/2}}+K(\phi)_{|X_{i-1/2}}}{\delta X^2}\right)p(X_i)\\&+\frac{K(\phi)}{\delta X^2}{}_{|X_{i-1/2}}\,p(X_{i-1})+\mathcal{O}\left(\delta X^2\right)=0.\end{aligned} \tag{55}$$

For every i, we want to solve

$$K(\phi)_{X_{i+1/2}}p(X_{i+1})-\left(K(\phi)_{X_{i+1/2}}+K(\phi)_{X_{i-1/2}}\right)p(X_i)+K(\phi)_{X_{i-1/2}}p(X_{i-1})=\mathcal{O}\left(\delta X^2\right). \tag{56}$$

From the above equation, we can calculate $p(X_i)$ at time $T+\delta T$, if we know $K(\phi)_{X_{i+1/2}}$. We choose

$$\phi_{X+\frac{1}{2}}(T)=\frac{1}{2}\left(\phi(X_i,T)+\phi(X_{i+1},T)\right)=\phi\left(X_{i+\frac{1}{2}},T\right)+\mathcal{O}\left(\delta X^2\right). \tag{57}$$

Then, considering a time-implicit scheme for the pressure and a time-explicit scheme for the porosity ϕ, we find that $p(X_i,T+\delta T)$ is the solution of the linear system:

$$\forall i\quad K\left(\phi^n_{X_{i+\frac{1}{2}}}\right)p^{n+1}_{i+1}-\left(K\left(\phi^n_{X_{i+\frac{1}{2}}}\right)+K\left(\phi^n_{X_{i-\frac{1}{2}}}\right)\right)p^{n+1}_i+K\left(\phi^n_{X_{i-\frac{1}{2}}}\right)p^{n+1}_{i-1}=0, \tag{58}$$

where $p^{n+1}_{i+1}=\bar{p}\left(X_{i+1},T^{n+1}\right)$, ($\bar{p}$ is the numerical approximation of p) and $T^{n+1}=T^n+\delta T^n$. The above linear system has a unique solution. We first applied a direct Gauss

solver to solve (58), which was replaced by a more efficient iterative method (incomplete LU BiConjugate gradient Squared solver) from the SLAP library (Greenbaum and Seager 1986). As an example, an invasion filtration was done to compare both solvers, using 300 cells. We found that the second method is three orders of magnitude faster. Larger contrasts are observed when the number of grid cells is increased. Equation 49 is solved for the time $T = T^{n+1}$.

We now turn to the solution of $\frac{\partial}{\partial T}\phi = 0$. This means that

$$\begin{aligned} &\forall i \quad \phi\left(X_i, T + \delta T\right) = \phi\left(X_i, T\right) \\ &\text{or} \qquad\qquad \phi_i^{n+\frac{1}{2}} = \phi_i^n. \end{aligned} \tag{59}$$

The solution of Eq. 50 at time $T^n + \delta T^n = T^{n+1}$ is indicated with superscript $n + \frac{1}{2}$. However, in order to distinguish between the solution of (49)+ (50)+ (51) at $T = T^{n+1}$, we have introduced this intermediate state $n + \frac{1}{2}$, which will serve as initial condition to solve (51) at the same time step. We solve

$$\frac{\partial}{\partial T}u + \frac{\partial}{\partial X}\left(\frac{u}{\phi}\right) = 0 \tag{60}$$

using the finite volume technique:

$$\begin{aligned} \forall i \quad \int_{T^n}^{T^{n+1}} \int_{M_i} \partial_T u + \int_{T^n}^{T^{n+1}} \int_{M_i} \partial_X \left(\frac{u}{\phi}\right) &= \int_{M_i} \left(u\left(T^{n+1}, X\right) - u\left(T^n, X\right)\right) \mathrm{d}X \\ &+ \int_{T^n}^{T^{n+1}} \left(\left(\frac{u}{\phi}\right)_{X_{i+\frac{1}{2}}}(T) - \left(\frac{u}{\phi}\right)_{X_{i-\frac{1}{2}}}(T)\right) \mathrm{d}T. \end{aligned} \tag{61}$$

We define an approximation of $u\left(T^{n+1}, X_i\right)$ by

$$u_i^{n+\frac{1}{2}} = \frac{1}{\delta X}\int_{M_i} u\left(T^{n+1}, X_i\right) \mathrm{d}X. \tag{62}$$

Then, we have

$$\delta X\left(u_i^{n+\frac{1}{2}} - u_i^n\right) + \int_{T^n}^{T^{n+1}} \left(\left(\frac{u}{\phi}\right)_{X_{i+\frac{1}{2}}}(T) - \left(\frac{u}{\phi}\right)_{X_{i-\frac{1}{2}}}(T)\right) \mathrm{d}T. \tag{63}$$

We approximate

$$\int_{T^n}^{T^{n+1}} \left(\frac{u}{\phi}\right)_{X+\frac{1}{2}}(T)\mathrm{d}T \simeq \delta T^n \frac{u_{i+\frac{1}{2}}^n}{\phi^{n+\frac{1}{2}}} \tag{64}$$

where we note

$$\frac{1}{2}\left(\phi_i^{n+\frac{1}{2}} + \phi_{i+1}^{n+\frac{1}{2}}\right) = \phi_{i+\frac{1}{2}}^{n+\frac{1}{2}}, \tag{65}$$

because of Eq. 59. We choose a first-order upstream approximation where

$$u_{i+\frac{1}{2}}^n = u_i^n. \tag{66}$$

If we choose

$$\frac{\delta T^n}{\delta X} \max\left(\frac{1}{\phi_{i+\frac{1}{2}}^{n+\frac{1}{2}}}, \frac{1}{\phi_{i-\frac{1}{2}}^{n+\frac{1}{2}}}\right) \leq 1, \tag{67}$$

which is the CFL condition, then it is possible to show that

$$\min\left(u_i^n, u_{i-1}^n\right) \leq u_i^{n+\frac{1}{2}} \leq \max\left(u_i^n, u_{i-1}^n\right). \tag{68}$$

The numerical scheme is then stable and reads

$$u_i^{n+\frac{1}{2}} = u_i^n + \frac{\delta T^n}{\delta X}\left(\frac{u_i^n}{\phi_{i+\frac{1}{2}}^n} - \frac{u_{i-1}^n}{\phi_{i-\frac{1}{2}}^n}\right). \tag{69}$$

Although it would be possible to use a second-order scheme, we decided here to minimise the numerical diffusion by using a high CFL condition (close to 1) and a very large number of grid cells, which is possible to do in one dimension without significantly increasing the computational cost.

To solve (51), we use the finite volume technique:

$$\begin{aligned}\frac{\partial}{\partial T}u = \frac{\partial}{\partial T}\phi \rightarrow \int_{M_i}\int_{T^n}^{T^{n+1}} \frac{\partial}{\partial T}u \mathrm{d}T\mathrm{d}X = \int_{M_i}\int_{T^n}^{T^{n+1}} \frac{\partial}{\partial T}\phi \mathrm{d}T\mathrm{d}X \\ \rightarrow u_i^{n+1} = \phi_i^{n+1} + \left(u_i^{n+\frac{1}{2}} - \phi_i^{n+\frac{1}{2}}\right)\end{aligned} \tag{70}$$

and

$$\begin{aligned}\phi_i^{n+1} &= \phi_i^{n+\frac{1}{2}} - \lambda L \int_{T^n}^{T^{n+1}} \frac{u}{\phi}\left(1 + b\left(\phi - \phi_0\right)\right)\mathrm{d}T \\ &= \phi_i^{n+\frac{1}{2}} - \lambda L \delta T^n \frac{u_i^{n+1}}{\phi_i^{n+1}}\left(1 + b\left(\phi - \phi_0\right)\right) + \mathcal{O}\left(\delta T^n\right).\end{aligned} \tag{71}$$

We then solve

$$\phi_i^{n+1} = \phi_i^{n+\frac{1}{2}} - \lambda L \delta T^n \frac{u_i^{n+1}}{\phi_i^{n+1}}\left(1 + b\left(\phi_i^{n+1} - \phi_0\right)\right). \tag{72}$$

We could have chosen

$$\phi_i^{n+1} = \phi_i^{n+\frac{1}{2}} - \lambda L \delta T^n \frac{u_i^{n+\frac{1}{2}}}{\phi_i^{n+\frac{1}{2}}}\left(1 + b\left(\phi_i^{n+\frac{1}{2}} - \phi_0\right)\right), \tag{73}$$

but the solution of (73) is conditionally stable, *i.e.* δT^n has to be small so that ϕ_i^{n+1} is physically relevant. In particular, δT^n has to scale as $\frac{1}{\lambda}$, which can be very limiting for large values of λ. ϕ_i^{n+1} is unconditionally stable when solving Eq. 72. Equation 72 is a non-linear equation of ϕ_i^{n+1}:

$$\phi_i^{n+1} = \phi_i^{n+\frac{1}{2}} - \lambda L \delta T^n \frac{\phi_i^{n+1} + \left(u_i^{n+\frac{1}{2}} - \phi_i^{n+\frac{1}{2}}\right)}{\phi_i^{n+1}} \left(1 + b\left(\phi_i^{n+1} - \phi_0\right)\right). \tag{74}$$

Equation 74 is solved using a quasi-Newton method.

Summarising, we have

1. linear system to solve for the pressure:

$$K_{i+\frac{1}{2}}^n p_{i+1}^{n+1} - \left(K_{i+\frac{1}{2}}^n + K_{i-\frac{1}{2}}^n\right) p_i^{n+1} + K_{i-\frac{1}{2}}^n p_{i-1}^{n+1} = 0. \tag{75}$$

2.

$$\begin{cases} u_i^{n+\frac{1}{2}} = u_i^n + \frac{\delta T^n}{\delta X}\left(\frac{u_i^n}{\phi^n_{i+\frac{1}{2}}} - \frac{u_{i-1}^n}{\phi^n_{i-\frac{1}{2}}}\right) \\ \phi_i^{n+\frac{1}{2}} = \phi_i^n \end{cases} \tag{76}$$

3. a non-linear scalar equation to solve

$$\begin{cases} \phi_i^{n+1} = \phi_i^{n+\frac{1}{2}} - \lambda L \delta T^n \frac{\phi_i^{n+1} + \left(u_i^{n+\frac{1}{2}} - \phi_i^{n+\frac{1}{2}}\right)}{\phi_i^{n+1}} \left(1 + b\left(\phi_i^{n+1} - \phi_0\right)\right) \\ u_i^{n+1} = \phi_i^{n+1} + \left(u_i^{n+\frac{1}{2}} - \phi_i^{n+\frac{1}{2}}\right) \end{cases} \tag{77}$$

δT^n is given by

$$\delta T^n \leq \min_i \left(\delta X \frac{1}{\phi^n_{i+\frac{1}{2}}}\right) \times C, \tag{78}$$

where $C \leq 1$.

The actual time t^n can be calculated using Eq. (47):

$$\frac{\partial}{\partial t} = \frac{L}{V_w}\frac{\partial}{\partial T} \tag{79}$$

$$\int_{t^n}^{t^{n+1}} \mathrm{d}t = t^{n+1} - t^n = \int_{T^n}^{T^{n+1}} \frac{L}{V_w(T)} \mathrm{d}T = \begin{cases} = \frac{L}{V_w}\left(T^{n+1} - T^n\right) & \text{constant flow rate} \\ \simeq \frac{L}{2}\left(\frac{1}{V_w(p^{n+1},\phi^n)} + \frac{1}{V_w(p^n,\phi^{n-1}))}\right) + \mathcal{O}\left((\delta T^n)^2\right) & \text{constant pressure.} \end{cases} \tag{80}$$

References

Bailey, L., Boek, E.S., Jacques, S., Boassen, T., Selle, O., Argillier, J-F., Longeron, D.: Particulate invasion from drilling fluids, SPE 54762, presented at the 1999 SPE European Formation Damage Conference in The Hague, The Netherlands, 31 May–1 June (1999)

Bailey, L., Boek, E.S., Jacques, S., Boassen, T., Selle, O., Argillier, J-F., Longeron, D.: Particulate invasion from drilling fluids. SPE J. **5**(4), 412–419 (2000)

Bailey, L., Meeten, G., Way, P.: Filtercake integrity and reservoir damage, SPE 39429. SPE International Symposium on Formation Damage Control, Lafayette, Louisiana, 18–19 February (1998)

Boek, E.S., van der Schoot, P.: Resolution effects in dissipative particle dynamics simulations. Int. J. Mod. Phys. C **9**, 1307–1318 (1998)
Boek, E.S., Venturoli, M.: Lattice-Boltzmann studies of fluid flow in porous media with realistic rock geometries. Comput. Math. Appl. **59**, 2305–2314 (2010)
Boek, E.S., Ladva, H.K.J., Crawshaw, J.P., Padding, J.T.: Deposition of colloidal asphaltene in capillary flow: experiments and mesoscopic simulation. Energy Fuels **22**, 805–813 (2008)
Boek, E.S., Padding, J.T., Headen, T.: Multi-scale simulation of asphaltene aggregation and deposition in capillary flow. Faraday Discuss. **144**, 271–284 (2010)
Boek, E.S., Wilson, A.D., Padding, J.T., Headen, T., Crawshaw, J.P.: Multi-scale simulation and experimental studies of asphaltene aggregation and deposition in capillary flow. Energy Fuels **24**, 2361–2368 (2010)
Dake, L.P.: Fundamentals of Reservoir Engineering. Elsevier, Amsterdam (2002)
Francis, P.: Dominating effects controlling the extent of drilling-induced formation damage. SPE 38182. SPE European Formation Damage Symposium, The Hague, The Netherlands, 2–3 June (1997)
Fordham, E.J., Hammond, P.S., Ladva, H.K.J., Schwartz, L., Wilkinson, D.: The early stages of drilling mud filtration on permeable rock. 6th IFP Exploration and Production Research Conference: Physical Chemistry of Colloids in Oil Production, 4–6 September 1991, St Raphael, France
Greenbaum, A., Seager, M.K.: http://www.netlib.org/slap/index.html. (1986)
Herzig, J.-P., Leclerc, D.M., Le Goff, P.: Flow of suspensions through porous media. Ind. Eng. Chem. **62**, 8–35
Ladva, H., Tardy, P., Howard, P., Dussan, E.: Multiphase flow and drilling fluid filtrate effects on the onset of production. SPE 58795, presented at 2000 SPE International Symposium on Formation Damage Control in Lafayette, 23–24 February (2000)
Manz, B., Gladden, LF., Alexander, P.: Flow and dispersion in porous media: Lattice-Boltzmann and NMR studies. AIChE J. **45**, 1845–1854 (1999)
Rege, S.D., Fogler, H.S.: Network model for straining dominated particle entrapment in porous media. Chem. Eng. Sci. **42**(7), 1553–1564 (1987)
Rege, S.D., Fogler, H.S.: A network model for deep bed filtration of solid particles and emulsion drops. AIChE J. **34**(11), 1761–1772 (1988)
Russel, W.B., Saville, D.A., Schowalter, W.R.: Colloidal Dispersions. Cambridge University Press, Cambridge (1995)
Schwartz, L.M., Wilkinson, D.J., Bolsterli, M., Hammond, P.: Particle filtration in consolidated granular systems. Phys. Rev. B **47**, 4953–4958 (1993)
Sharma, M.M., Yortsos, Y.C.: Transport of particulate suspensions in porous media: model formulation. AIChE J. **33**(10), 1636–1643 (1987a)
Sharma, M.M., Yortsos, Y.C.: A network model for deep bed filtration processes. AIChE J. **33**(10), 1644–1653 (1987b)
Sharma, M.M., Yortsos, Y.C.: Fines migration in porous media. AIChE J. **33**(10), 1654–1662 (1987c)
Stephan, E.A., Chase, G.G.: Development of volume-average theory for deep-bed filtration. AIChE J. **46**, 1918–1926 (2000)
Tardy, P., Quintard, M.: Solving stiff mass transfers in computational multiphase flow models: numerical stability and spurious solutions. Comput. Geosci. **3**, 161–183 (1999)
Vardoulakis, I., Stavropoulou, M., Papanastasiou, P.: Hydro-mechanical aspects of the sand production problem. Transp. Porous Media **22**, 225–244 (1996)
Wennberg, K.E., Batrouni, G.G., Hansen, A., Horsrud, P.: Band formation in deposition of fines in porous media. Transp. Porous Media **25**, 247–273 (1996)